Energy 65 (2014) 412–418

Contents lists available at ScienceDirect

Energy

journal homepage: www.elsevier.com/locate/energy

# $k$–$\omega$ SST (shear stress transport) turbulence model calibration: A case study on a small scale horizontal axis wind turbine

P.A. Costa Rocha [a], H.H. Barbosa Rocha [a,*], F.O. Moura Carneiro [a], M.E. Vieira da Silva [b], A. Valente Bueno [c]

[a] Laboratory of Aerodynamics and Fluid Mechanics (LAero), Department of Mechanical Engineering, Federal University of Ceará, Campus do Pici 715, Fortaleza, CE 60440-554, Brazil

[b] Solar Energy and Natural Gas Laboratory, Campus do Pici, Bl. 718, Fortaleza, CE 60440-554, Brazil

[c] Laboratory of Internal Combustion Engines, Department of Mechanical Engineering, Federal University of Ceará, Campus do Pici 715, Fortaleza, CE 60440-554, Brazil

ARTICLE INFO

*Article history:*
Received 23 July 2013
Received in revised form
22 October 2013
Accepted 18 November 2013
Available online 18 December 2013

*Keywords:*
Aerodynamic performance
$k$–$\omega$ SST turbulence model
Model calibration
Small scale HAWT
Wind energy

ABSTRACT

This work deals with a computational investigation emphasized on the calibration of a turbulence model regarding to the operational capability of a SS-HAWT (small-scale horizontal axis wind turbine). Experimental field tests were carried out to collect data to evaluate the performance (power) coefficient, $C_p$, as a function of the tip-speed ratio, $\lambda$. The prototype examined was a three-bladed wind turbine (NACA (National Advisory Committee for Aeronautics) 0012 profile) designed for fixed tip-speed ratio (with $\lambda = 5$), constructed and operated at the Federal University of Ceará. The maximum value experimentally achieved for $C_p$ was about 14%. The $k$–$\omega$ SST (shear stress transport) turbulence model, solved by the open source CFD (computational fluid dynamics) toolbox OpenFOAM (Open Source Field Operation and Manipulation), assessed the wind turbine performance. The experimental data information obtained reporting the aerodynamic performance of the SS-HAWT prototype was required to calibrate the model. The turbulence intensity and the characteristic length were studied in terms of the $\beta^*$ parameter. The power coefficient numerically predicted tends to agree with the experimental assessment. The variation of $\beta^*$ mainly affects viscous friction over the blades.



## 1. Introduction

SS-HAWTs (small scale horizontal axis wind turbines), which should be safe enough and easy to run for self-sufficient and independent power production purposes [1], are becoming a research topic of active interest [2–6]. These machines rely solely on the torque produced by the wind acting on the blades. This happens because, in general, they are not provided with a generator operating as a motor to start and accelerate the rotor when the wind is strong enough to begin producing power [7]. Particularly, the blades of an SS-HAWT should start rotating at the lowest possible wind speed in order to extract the maximum possible power [8], without necessarily the best of wind conditions [9].

In some cases, the investigation of SS-HAWTs should (or must) include the CFD (computational fluid dynamics) analysis/design tool. The criterion of success can be taken in terms of how well the results of numerical simulation agree with experiments (in cases where careful laboratory experiments can be established), and how well the simulations can predict highly complex phenomena (that necessarily cannot be isolated in the laboratory) [10]. It is well known that CFD cannot reproduce physics that are not properly included in the formulation of the problem, which is the case in the study of turbulence [11]. For instance, the experimental data of the NREL (National Renewable Energy Laboratory) phase VI blade [12–14] were used to validate a numerical model and to apply this calibrated model in the performance analysis of hypothetical blunt blades with thicknesses distinct from the original (experimental) blades [15]. To achieve this purpose, it was employed the software FLUENT as a solver and ICEM-CFD for the mesh generation. The simulation results obtained with FLUENT agreed with experimental data. In general, the numerical simulations did not indicate significant losses over the blades' performance in parallel with their structural reinforcement.

Especially for aeronautical flows, turbulence models of the $k$–$\omega$ type, are very popular [16]. Indeed, this is currently a wide-open

* Corresponding author. Tel./fax: +55 85 3366 9881.
*E-mail addresses:* helio.rocha@alu.ufc.br, helio.rocha@creace.org.br (H.H. B. Rocha).

0360-5442/$ – see front matter © 2013 Elsevier Ltd. All rights reserved.
http://dx.doi.org/10.1016/j.energy.2013.11.050

**Nomenclature**

| | |
|---|---|
| $a_1$ | turbulence modeling constant |
| $c_a$ | airfoil chord length (m) |
| $C_l$ | lift coefficient |
| $C_p$ | power coefficient |
| $D$ | turbine diameter (m) |
| $F_1$ | blending function |
| $F_2$ | blending function |
| $I$ | free-stream turbulence intensity (%) |
| $k$ | specific turbulent kinetic energy (m$^2$ s$^{-2}$) |
| $M_p$ | moment due to pressure forces (kg m$^2$ s$^{-2}$) |
| $M_v$ | moment due to viscous forces (kg m$^2$ s$^{-2}$) |
| $N$ | number of blades |
| $P_k$ | rate of production of $k$ (kg m$^{-1}$ s$^{-3}$) |
| $\tilde{P}_k$ | effective rate of production of $k$ (kg m$^{-1}$ s$^{-3}$) |
| $P_s$ | shaft input power (kg m$^2$ s$^{-3}$) |
| $P_\omega$ | rate of production of $\omega$ (kg m$^{-3}$ s$^{-2}$) |
| $r$ | radial blade position (m) |
| $R$ | blade radius (m) |
| $\mathbf{S}$ | invariant measure of the strain rate (s$^{-1}$) |
| $S_{ij}$ | mean rate of deformation component (s$^{-1}$) |
| $T$ | torque (kg m$^2$ s$^{-2}$) |
| $U$ | incident free-stream airflow (m s$^{-1}$) |
| $y$ | shortest distance to the near wall (m) |
| $\beta$ | turbulence modeling constant |
| $\beta^*$ | turbulence modeling constant |
| $\gamma$ | turbulence modeling constant |
| $\delta_{ij}$ | Kronecker delta function |
| $\lambda$ | tip-speed ratio |
| $\mu_t$ | eddy viscosity (kg m$^{-1}$ s$^{-1}$) |
| $\nu_t$ | kinematic eddy viscosity (m$^2$ s$^{-1}$) |
| $\rho$ | density (kg m$^{-3}$) |
| $\sigma_k$ | turbulence modeling constant |
| $\sigma_\omega$ | turbulence modeling constant |
| $\tau_{ij}$ | turbulent Reynolds stress tensor (kg m$^{-1}$ s$^{-2}$) |
| $\omega$ | specific turbulent dissipation rate (s$^{-1}$) |
| $\Omega$ | angular speed of the rotor (rad s$^{-1}$) |
| $\mathcal{K}_e$ | kinetic energy flux (kg m$^2$ s$^{-3}$) |
| $\mathfrak{L}_t$ | turbulent length scale (m) |
| $\mathfrak{X}$ | cross-diffusion term (kg m$^{-1}$ s$^{-2}$) |
| BEM | blade element momentum |
| CFD | computational fluid dynamics |
| HAWT | horizontal axis wind turbine |
| NACA | National Advisory Committee for Aeronautics |
| OpenFOAM | Open Source Field Operation and Manipulation |
| RANS | Reynolds-averaged Navier–Stokes (equations) |
| SS-HAWT | small scale horizontal axis wind turbine |
| SST | shear stress transport |

area of CFD research, which some of the efforts related to SS-HAWT/HAWT are reported in Refs. [17,18].

## 2. SS-HAWT experimental procedures

### 2.1. Aerodynamic design

The wind turbine investigated was a three-bladed upwind turbine rotor (with fixed blades on the hub) and free (passive) yaw control system with a movable tail vane. The BEM (blade element momentum) theory was employed to design the blades for the SS-HAWT prototype. The aerodynamic profile of the airfoils that comprised the blades was the symmetrical NACA (National Advisory Committee for Aeronautics) 0012 (maximum thickness of 12% compared to the chord length). The radius of the blades is equal to 1.5 m. The rotor was mounted on a tower pole at an elevation of 5 m above the ground (in open field) at the Federal University of Ceará.

In practical terms, the original plain-form of the design theory (described in Ref. [19]) is simplified (what removes a lot of material close to the root) and the expression adopted in the design, as suggested by Burton [19], assumes the form of Eq. (1):

$$\frac{c_a}{R} = \frac{8}{9 \cdot 0.8\lambda}\left[2 - \frac{\lambda\left(\frac{r}{R}\right)}{0.8\lambda}\right]\frac{2\pi}{C_l\lambda N}, \tag{1}$$

where $c_a$ is the airfoil chord length (m), $R$ denotes the blade radius (m), $\lambda$ expresses the tip-speed ratio, $r$ represents the radial blade position (m), $C_l$ is the profile lift coefficient and $N$ is the number of blades. The 0.8 in Eq. (1) refers to the 80% point between the target points. Further details on wind turbine design and construction followed instructions provided in Ref. [20].

### 2.2. Prototype field tests

To obtain the shaft power, the wind turbine prototype was instrumented in order to measure directly the rotation and torque. The rotational speed of the main mechanical shaft was measured using a tachometer model TADIG-C1 (T&S Equipamentos eletrônicos, Brazil) with maximum estimated error equal to ±0.23%. The torque measurement was made via torque transducer (T22 HBM, Germany), with nominal (rated) torques up to 1 kNm, accuracy class 0.5, and ±0.2% of sensitivity tolerance for voltage and/or current output. Flux measurements (wind velocity) were realized using WindMaster 1590 PK-20 (Gill, United Kingdom) pulse-based ultrasonic anemometer mounted 4 m far from the wind turbine and at an elevation of 4.5 m above the ground. The anemometer can measure a maximum wind speed of 45 m s$^{-1}$ with a resolution of 0.01 or 0.001 m s$^{-1}$ and accuracy (12 m s$^{-1}$) >1.5% RMS (Root Mean Squared). Data were logged on EL005 Enviromon and EL037 data loggers (Pico technology, United Kingdom) and stored on a personal computer. The experimental data acquisition system and the measuring station/prototype under test are depicted in Fig. 1.

The power coefficient $C_p$, which represents the ratio between $P_s$, the shaft input power (kg m$^2$ s$^{-3}$), and $\mathcal{K}_e$, the kinetic energy flux (kg m$^2$ s$^{-3}$), both experimentally measured, was evaluated from Eq. (2):

$$C_p = \frac{P_s}{\mathcal{K}_e} = \frac{\Omega T}{0.5\rho\pi R^2 U^3}, \tag{2}$$

where $\Omega$ is the angular speed of the rotor (rad s$^{-1}$), $T$ represents the torque (kg m$^2$ s$^{-2}$), $\rho$ is the air density (kg m$^{-3}$), and $U$ denotes the incident free-stream airflow (m s$^{-1}$). The tip-speed ratio $\lambda$ is expressed by Eq. (3):

$$\lambda = \frac{\Omega R}{U}. \tag{3}$$

It is useful to note that equivalent experimental approaches were employed in investigations carried out in wind tunnels: a study on the aerodynamic characteristics of a HAWT designed according to the BEM theory [21], given that the results are based on the power evaluated from data obtained via torque and rotation measurements, and a similar work dealing with telescopic blades [22].

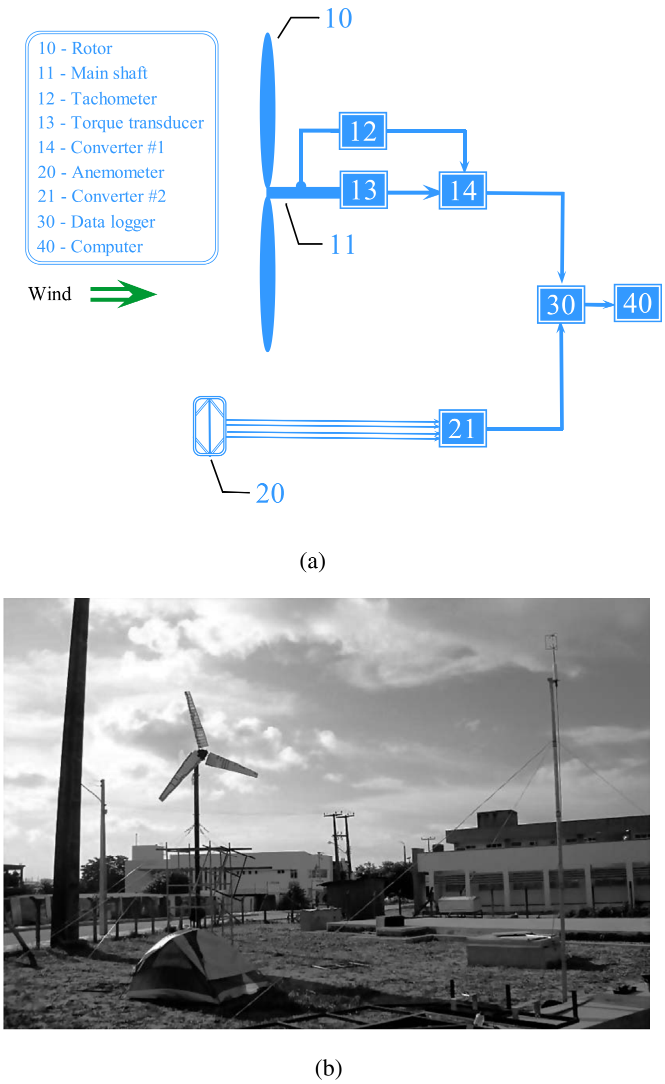


**Fig. 1.** SS-HAWT under test: (a) schematic of the experimental data acquisition system and (b) measuring station at Federal University of Ceará.

## 3. *k*–*ω* SST (shear stress transport) turbulence model

Menter's $k$–$\omega$ shear stress transport (SST) model [23–26] comprises two equations [23,27]:

- one for $k$, the specific turbulent kinetic energy ($m^2\ s^{-2}$) (Eq. (4)):

$$\frac{\partial}{\partial t}(\rho k) + \frac{\partial}{\partial x_i}(U_i \rho k) = \frac{\partial}{\partial x_j}\left(\mu_k \frac{\partial}{\partial x_j} k\right) + \tilde{P}_k - \beta^* \rho \omega k, \tag{4}$$

- and one for $\omega$, the specific turbulent dissipation rate ($s^{-1}$) (or specific turbulent frequency) (Eq. (5)):

$$\frac{\partial}{\partial t}(\rho\omega) + \frac{\partial}{\partial x_i}(U_i \rho \omega) = \frac{\partial}{\partial x_j}\left(\mu_\omega \frac{\partial}{\partial x_j}\omega\right) + P_\omega - \beta\rho\omega^2 + 2\rho(1-F_1)\frac{1}{\omega}\frac{1}{\sigma_{\omega,2}}\frac{\partial}{\partial x_j}k\frac{\partial}{\partial x_j}\omega. \tag{5}$$

The effective viscosities ($kg\ m^{-1}\ s^{-1}$) are given by Menter [25]:

$$\mu_k = \mu + \mu_t \frac{1}{\sigma_k}, \tag{6}$$

$$\mu_\omega = \mu + \mu_t \frac{1}{\sigma_\omega}, \tag{7}$$

where $\mu_t$ is the modified eddy (or turbulent) viscosity ($kg\ m^{-1}\ s^{-1}$), and $\sigma_\chi$ ($\chi = k;\omega$) are diffusion constants of the model. The Reynolds stresses $\tau_{ij}$ ($kg\ m^{-1}\ s^{-2}$) are computed as usual in two-equation models with the Boussinesq expression [25,27]:

$$\tau_{ij} = -\rho\overline{U_i' U_j'} \tag{8a}$$

$$= 2\mu_t S_{ij} - \frac{2}{3}\rho k \delta_{ij}. \tag{8b}$$

In Eq. (8b), $S_{ij}$ represents the mean rate of deformation component ($s^{-1}$) and $\delta_{ij}$ is the Kronecker delta function. $P_\omega$, the rate of production of $\omega$ ($kg\ m^{-3}\ s^{-2}$), is given by the Eq. (9) [27]:

$$P_\omega = \gamma\left[2\rho S_{ij} \cdot S_{ij} - \frac{2}{3}\rho\omega\left(\frac{\partial}{\partial x_j}U_i\right)\delta_{ij}\right], \tag{9}$$

where $\gamma$ is a model constant.

### 3.1. Updated turbulence model constants and limiting

The constants in the $k$–$\omega$ SST model are blended values of the standard $k$–$\omega$ and $k$–$\varepsilon$ parameters calculated from the blending function $F_1$ [23], as defined by Eq. (10):

$$F_1 = \tanh\left(\left\{\min\left[\max\left(\frac{\mathfrak{L}_t}{y};\frac{500\nu_t}{y^2\omega}\right);\frac{4\rho\sigma_{\omega,2}k}{\mathfrak{X}y^2}\right]\right\}^4\right), \tag{10}$$

whereas $F_1$ is limited (varies) from unity at the wall to zero outside wall boundary layers. The first argument in Eq. (10), $\mathfrak{L}_t$ [$=k^{1/2}/(0.09\omega)$], represents the turbulent length scale (m), divided by $y$, the shortest distance to the near wall (m). The positive portion of $\mathfrak{X}$, the cross-diffusion term ($kg\ m^{-1}\ s^{-2}$), presented in Eq. (5) is limited as [26]:

$$\mathfrak{X} = \max\left(2\rho\frac{1}{\omega}\frac{1}{\sigma_{\omega,2}}\frac{\partial}{\partial x_i}k\frac{\partial}{\partial x_i}\omega; 10^{-10}\right). \tag{11}$$

Each coefficient of the Menter's model ($\varphi \equiv \sigma_k, \sigma_\omega, \beta, \gamma$) is evaluated from Eq. (12) [24]:

$$\varphi = \varphi_1 F_1 + \varphi_2(1-F_1), \tag{12}$$

where the subscript 1 (in $\varphi$) is related to the adjusted $k$–$\omega$ model and the subscript 2 is connected with the standard $k$–$\varepsilon$ model, whose constants values are given as follows [23]:

$$\sigma_{k,1} = \frac{1}{0.85034}, \quad \sigma_{k,2} = 1.0,$$

$$\sigma_{\omega,1} = 2.0, \quad \sigma_{\omega,2} = \frac{1}{0.85616},$$

$$\beta_1 = \frac{3}{40}, \quad \beta_2 = 0.0828, \quad \beta^* = \frac{9}{100}, \quad \kappa = 0.41,$$

$$\gamma_1 = \left(\frac{\beta_1}{\beta^*}\right) - \left(\frac{\sigma_{\omega,1}\kappa^2}{(\beta^*)^{1/2}}\right) = 0.5532,$$

$$\gamma_2 = \left(\frac{\beta_2}{\beta^*}\right) - \left(\frac{\sigma_{\omega,2}\kappa^2}{(\beta^*)^{1/2}}\right) = 0.44.$$

Improved performance in flows with adverse pressure gradients and wake regions are obtained by limiting the eddy viscosity [23,27]:

$$\mu_t \frac{1}{\rho} = \frac{a_1 k}{\max(a_1\omega, \mathbf{S}F_2)} = \nu_t, \tag{13}$$

given that $\mathbf{S} = (2S_{ij}S_{ij})^{1/2}$ is the invariant measure of the strain rate, $a_1$ (=0.31) is a constant, $\nu_t$ is the kinematic eddy viscosity ($m^2\ s^{-1}$) and $F_2$ is a blending function [23] given by the Eq. (14):

$$F_2 = \tanh\left(\left[\max\left(2\frac{\mathfrak{L}_t}{y}; \frac{500\nu_t}{y^2\omega}\right)\right]^2\right). \tag{14}$$

For other regions of the boundary layer, the eddy viscosity can be evaluated according to Eq. (15)

$$\mu_t = \rho\left(\frac{k}{\omega}\right). \tag{15}$$

To prevent the build-up of turbulence in stagnation regions, $\tilde{P}_k$, the effective rate of production of ($kg\ m^{-1}\ s^{-3}$), is limited as follows [26]:

$$\tilde{P}_k = \min(P_k; 10\beta^*\rho k\omega), \tag{16}$$

where $P_k$, the rate of production of ($kg\ m^{-1}\ s^{-3}$), is expressed by the Eq. (17) [27]:

$$P_k = 2\mu_t S_{ij} \bullet S_{ij} - \frac{2}{3}\rho k\left(\frac{\partial}{\partial x_j}U_i\right)\delta_{ij}. \tag{17}$$

## 4. Numerical setup

The frozen rotor approach was taken into account in this study. It consists of a steady-state formulation in which the rotor and the fluid (air) are fixed with respect to each other. The computational fluid dynamics code used for turbulence model simulation was OpenFOAM (Open Source Field Operation and Manipulation)[1] v.1.7.1 [28,29]. All the simulations were carried out with the "simpleFoam" solver, which is a steady state, incompressible solver. This solver has full access to all the turbulence models in the "incompressibleTurbulenceModels" library of the standard OpenFOAM release. The generalized fully second-order setup was used for all simulations. The NVD (normalized variable diagram) type differencing scheme – GAMMA [30] with $\gamma_{NVD} = 1.0$ was applied for all convective terms approximation. All other inviscid terms and the pressure gradient were approximated with a fourth order accuracy. The relaxation parameters were set to the default value of 0.04 for pressure and of 0.06 for the other prognostic variables. For the spatial discretization of differential operators, the Gaussian integration was used with different interpolation schemes.

### 4.1. Boundary conditions

The specification of $I$, a free-stream turbulence intensity (%), can be given as follows in Eq. (18) [27]:

$$k = \frac{3}{2}(IU)^2. \tag{18}$$

The turbulent frequency term can be determined by the Eq. (19) [11,27]:

$$\omega = \frac{k^{1/2}}{\mathfrak{L}_t}, \tag{19}$$

where $\mathfrak{L}_t$ denotes the turbulent length scale (m).

For the boundary conditions, the following criteria were observed:

- The inlet free-stream speed was based on the average of the values obtained in the field, *i.e.*, 2.5 $m\ s^{-1}$. On the turbine, the "rotatingWallVelocity" condition (which evaluates the velocity fields over a solid surface, using a priori rotation condition) was employed, based on experimental $\lambda$ (=7.85). On outlet, the "zeroGradient" condition was applied.
- For pressure, "zeroGradient" conditions were used in the inlet and on the turbine; 0 $kg\ m^{-1}\ s^{-2}$ (gauge) was specified at the outlet.
- $k$ and $\omega$, respectively expressed by the Eqs. (18) and (19), were used at the inlet of the domain and on the turbine. The "zeroGradient" condition was applied at the outlet.
- The "slip" condition was employed in the physical contour of the domain.

### 4.2. Mesh generation

An optimum solution to this problem is expected to be reasonably complex and will require the creation of a mesh representative of the flow. Primarily, it was intended to determine the geometrical dimensions of the domain (a cylinder that includes the wind turbine), since it must adequately represent the aerodynamic effects of the expansion cone. Values ranging from 10 to 90 m downstream and 5 to 30 m upstream were considered during the determination of the domain's length. It was concluded 30 m as an optimal value for both upstream as downstream. The diameter of the domain was set to 12 m (or 4 $D$, where $D$ is the turbine diameter (m)) and the diameter of the inner cylinder (more refined) was set equal to 6 m (or 2$D$). By using streamlines, it was shown that this inner cylinder covers all the wind turbine's expansion cone.

The computational mesh generated from 1.6 to 3.2 million hexahedral elements refined horizontally. A grid sensitivity analysis was carried out to estimate the solution error associated to the discretization. Considering all the mesh's range analyzed, it was not verified significant variation on the results for $C_p$.

## 5. Experimental results and comparison to numerical simulation

This section provides a comparison between the experimental measurements and the computational predictions carried out to understand some of aerodynamic aspects of the wind turbine prototype.

The prototype designed, constructed and operated at the Federal University of Ceará was a three-bladed (NACA 0012 profile) fixed tip-speed ratio ($\lambda = 5$), as described in Section 2. As shown in Fig. 2(a), the power coefficient ($C_p$) plotted against the tip-speed ratio ($\lambda$) generated a scatter plot. These data were calculated from experimental measurements of the mechanical shaft rotational speed, torque and wind speed. Fig. 2(b) illustrates the average power coefficient for $\lambda$ intervals equal to 0.5. Efficiencies in the order of 10% were obtained in regimes close to the projected tip-speed ratio, with a peak of about 14% observed in $\lambda = 7.25$. It can be

[1] http://www.openfoam.com.

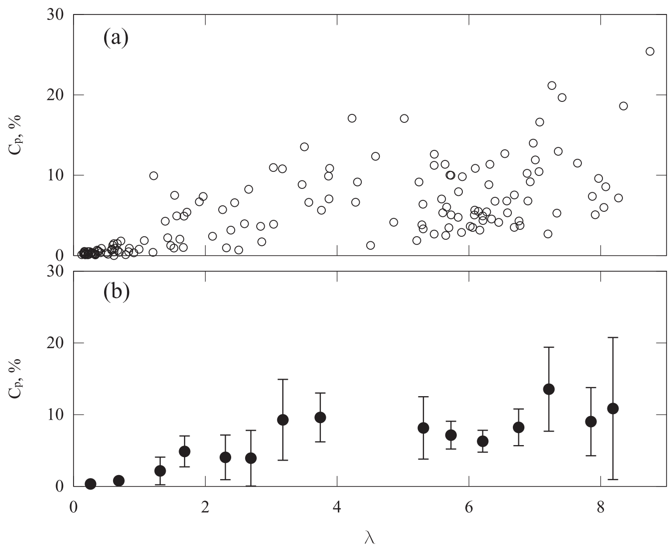


**Fig. 2.** Scatter plot of power coefficient $C_p$ vs. tip-speed ratio $\lambda$ (a) as experimentally observed and (b) considering 95% confidence intervals.

seen that there is a natural gain in turbine's efficiency in the range $0 < \lambda < 4$. This increase in the turbine performance can be attributable to the reduction of stall on the blade, that occurs at low revs (at high angles of attack). Near the design's tip-speed ratio, the turbine reaches its regular regime of operation, in which the blades have not significant stalled sections. However, as the $\lambda$ increases, the efficiency does not grow due to the adverse effect of the drag, which becomes considerable. The intervals shown in Fig. 2(b) represent the 95 confidence taken from a Student's *t*-distribution.

The experimental field data about the power coefficient were required to verify the simulation model. Model calibration here refers to minimize the discrepancy between the simulation model adopted and the actual physical system (real gathered data). Sensitivity tests to the numerical parameters (presented in Figs. 3 and 4) were carried out for the particular value of $\lambda = 7.85$. This was due to the fact that, at this tip-speed ratio, there is a clear assurance that the blades do not have considerable stalled regions, which would hinder the reliability of the numerical results, given the difficulty by the turbulence models in predicting flow separation [11].

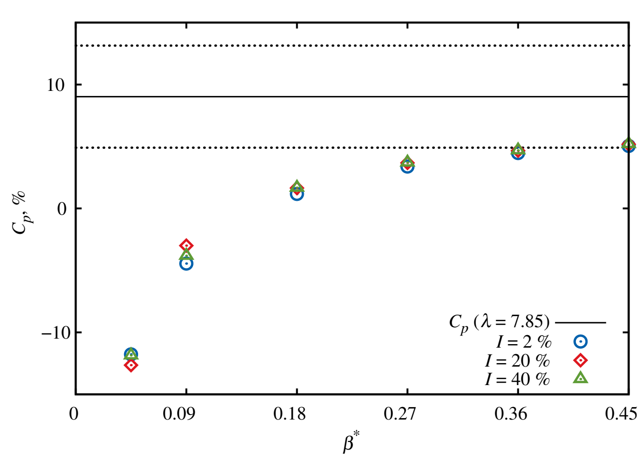


**Fig. 3.** Numerical results for power coefficient $C_p$ vs. $k$–$\omega$ SST model parameter $\beta^*$ for discrete turbulence intensities values compared to experimental measurements (solid line) for $\lambda = 7.85$. The 95% confidence interval related to experimental data is depicted by dotted lines.

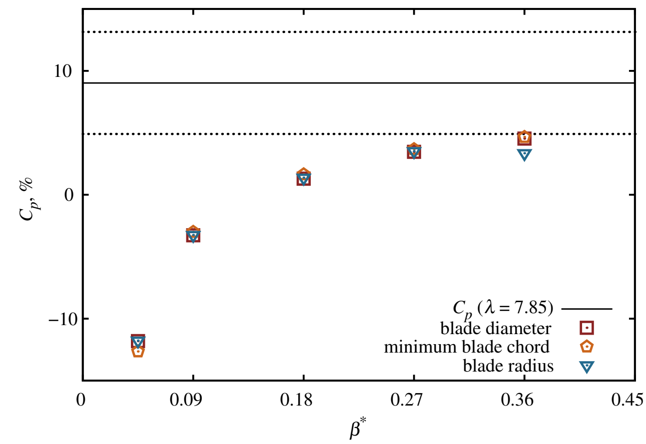


**Fig. 4.** Numerical results for power coefficient $C_p$ vs. $k$–$\omega$ SST model parameter $\beta^*$ for different turbulence characteristic lengths compared to experimental measurements (solid line) for $\lambda = 7.85$. The 95% confidence interval related to experimental data is depicted by dotted lines.

In the simulations' setup, values of the boundary conditions for the variables are required. In the present problem, most of these variables have direct physical meaning (velocity, pressure). However, the variables $k$ and $\omega$ are fundamental for the turbulence model and cannot be directly measured. Hence, the variables $I$ and $\mathfrak{L}_t$ that have direct physical meaning and directly impact on the calculation of $k$–$\omega$ (according to Eqs. (18) and (19)) are employed. With the experimental field data, the value of turbulence intensity value can be estimated. In turn $\mathfrak{L}_t$ now follows the geometric characteristics of the addressed proposition. With these values, the boundary conditions of $k$ and $\omega$ can be determined, enabling the numerical solution of the problem.

To study their influence in the model, at first the parameter $I$ was set with values 2%, 20% and 40%, then $\mathfrak{L}_t$ was set equal to three values: (1) the blade diameter, (2) the minimum blade chord and (3) the blade radius. Both turbulence intensity and characteristic length scale parameters were evaluated as a function of $\beta^*$, a constant of the $k$–$\omega$ SST turbulence model. The model's calibration performance was judged by visual comparison between experimental data/simulations results via graphs.

Fig. 3 represents the influence of the turbulence intensity and $\beta^*$ in the performance predicted by numerical solution. For the selected values of $\beta^*$ ($\beta^* = 0.09\xi$, $\xi = 0.5, 1, 2, 3, 4, 5$) there was no significant variation in performance of the blade by varying the intensity of turbulence. With the variation of $\beta^*$, it is observed a significant increase in the efficiency of the blade, starting from negative values (at which in practice the turbine would not work) to positive values getting inside (agreeing with) the confidence interval value of the experimental result.

Fig. 4 shows results similar to those observed in Fig. 3. This time is being tested the sensitivity for the characteristic length concomitant with the component $\beta^*$. Again the results were insensitive to variations of the characteristic length whereas there is a clear increase in efficiency with increasing $\beta^*$, *i.e.*, an agreement between the experimental and numerical results.

Fig. 5 is a representative detail of Fig. 3. The performance of the blade was separated into the effects of the moment due to viscous forces $M_v$ and the moment due to pressure forces $M_p$. It can be seen that with the increase of $\beta^*$, there is a significant change (decrease) in the moment component related to viscosity (Fig. 5(a)). Conversely, the same is not observable for the moment due to the effects of pressure, which practically remains constant (Fig. 5(b)).

As indicated by the results, the variation of $\beta^*$ directly impacted the turbulence effects relevant to the model. Therefore, it can be

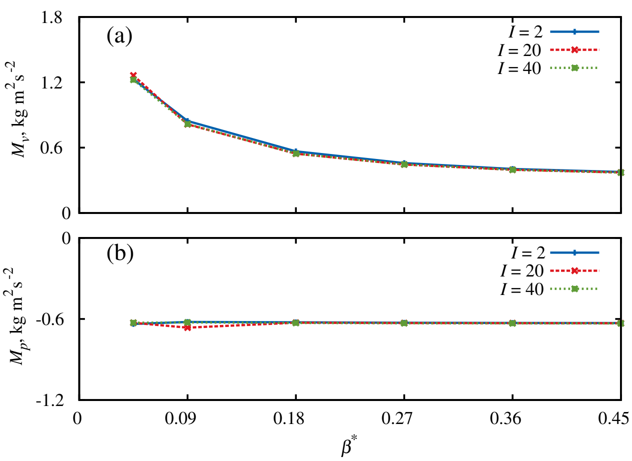


**Fig. 5.** Numerical results for (a) $M_v$ and (b) $M_p$ vs. $k$–$\omega$ SST model parameter $\beta^*$ for different values of turbulence intensity ($I = 2\%$, 20%, 40%).

seen that the impact of the turbulence in the RANS (Reynolds-averaged Navier—-Stokes) model, which in essence is a variation of the apparent viscosity, was significantly affected by the change of $\beta^*$. This fact becomes clearer if it is found that the change in $\beta^*$ practically impacted only surface effects, evidenced by viscous friction on the blades' surface. It is then observed that the model calibration succeeded probably owing to the viscous effects on the blades. This information proves itself very important since it can be obtained from negative (unrealistic) to positive values of efficiency and within the confidence interval of the experimental results as shown in Figs. 3 and 4.

A similar study was conducted with a VAWT (vertical axis wind turbine) [31], in which the realizable $k$–$\varepsilon$ model [32] was employed. Accordingly, $C_\mu$ (a critical coefficient of the realizable $k$–$\varepsilon$ model, and equivalent to the $\beta^*$ tested in the present work) is expressed as a function of mean flow and turbulence properties, rather than assumed to be constant as in the standard model.

## 6. Conclusion

A three-bladed (NACA 0012 profile) fixed tip-speed ratio ($\lambda = 5$) SS-HAWT was designed, constructed and operated at the Federal University of Ceará. The experimental field data made available for aerodynamic performance characteristic ($C_p$ vs. $\lambda$) was required to calibrate the $k$–$\omega$ SST turbulence model under frozen rotor regime. The following conclusions could be drawn:

- The turbulence intensity did not impact on the calibration of the model, for the same values of $\beta^*$, the results for $I = 2\%$, 20%, and 40% are almost the same and tends to coincide as the value of $\beta^*$ increases.
- Similarly, the turbulence characteristic length scale $\mathfrak{L}_t$ (blade diameter, minimum blade chord, blade radius) did not affect the calibration results.
- Presumable due to viscous effects, the $\beta^*$ coefficient, that explicitly appears in the equation for the $k$ (Eq. (4)) and implicitly in the $\omega$ equation (Eq. (5)), seems to have a relevant role in the turbulence model calibration.
- The $k$–$\omega$ SST turbulence model was calibrated with $\beta^* = 0.45$ for the specified case.

## Acknowledgments

This research was jointly supported by the Fundação Cearense de Apoio ao Desenvolvimento Científico e Tecnológico (FUNCAP), the Coordenação de Aperfeiçoamento de Pessoal de Nível Superior (CAPES), and the Conselho Nacional de Desenvolvimento Científico e Tecnológico (CNPq), Brazilian governmental agencies. Useful comments and suggestions from anonymous referees effectively helped the enhancement of this paper. Their contribution is gratefully acknowledged.

## References

[1] Balduzzi F, Bianchini A, Ferrari L. Microeolic turbines in the built environment: influence of the installation site on the potential energy yield. Renew Energy 2012;45:163–74.
[2] Lanzafame R, Messina M. Power curve control in micro wind turbine design. Energy 2010;35(2):556–61.
[3] Shen X, Zhu X, Du Z. Wind turbine aerodynamics and loads control in wind shear wow. Energy 2010;36(3):1424–34.
[4] Trivellato F, Battisti L, Miori G. The ideal power curve of small wind turbines from field data. J Wind Eng Ind Aerod 2012;107–108:263–73.
[5] Meyer DG, Srinivasan S, Semrau G. Dynamic wind estimation based control for small wind turbines. Renew Energy 2013;50:259–67.
[6] Simic Z, Havelka JG, Vrhovcak MB. Small wind turbines – a unique segment of the wind power market. Renew Energy 2013;50:1027–36.
[7] Wright AK, Wood D. The starting and low wind speed behaviour of a small horizontal axis wind turbine. J Wind Eng Ind Aerod 2004;92:1265–79.
[8] Ameku K, Nagai BM, Roy JN. Design of a 3 kW wind turbine generator with thin airfoil blades. Exp Therm Fluid Sci 2008;32:1723–30.
[9] Singh RK, Ahmed MR. Blade design and performance testing of a small wind turbine rotor for low wind speed applications. Renew Energy 2013;50:812–9.
[10] Sethian JA. Computational fluid dynamics. In: National Science Foundation (U.S.), editor. Blue Ribbon Panel on high performance computing. From desktop to teraflop: exploiting the U.S. lead in high performance computing. Washington: National Science Foundation; 1993.
[11] Wilcox D. Turbulence modeling for CFD. 3th ed. La Cañada: DCW Industries; 2006.
[12] Giguere P, Selig MS. Design of a tapered and twisted blade for the NREL combined experiment rotor. NREL/SR-500e26173; 1999.
[13] Simms D, Schreck S, Hand M, Fingersh LJ. NREL unsteady aerodynamics experiment in the NASA-Ames wind tunnel: a comparison of predictions to measurements. NREL/TP-500e29494; 2001.
[14] Hand MM, Simms DA, Fingersh LJ, Jager DW, Contrell JR, Schreck SJ, et al. Unsteady aerodynamics experiment phase VI: wind tunnel test configurations and available data campaigns. NREL/TP-500e29955; 2001.
[15] Lee SG, Park SJ, Lee KS, Chung C. Performance prediction of NREL (National Renewable Energy Laboratory) phase VI blade adopting blunt trailing edge airfoil. Energy 2012;47(1):47–61.
[16] Knopp T, Eisfeld B, Calvo JB. A new extension for $k$-$\omega$ turbulence models to account for wall roughness. Int J Heat Fluid Flow 2009;30:54–65.
[17] Abe K, Nishida M, Sakurai A, Ohya Y, Kihara H, Wada E, et al. Experimental and numerical investigations of flow fields behind a small wind turbine with a flanged diffuser. J Wind Eng Ind Aerod 2005;93:951–70.
[18] Li Y, Paik K-J, Xing T, Carrica PM. Dynamic overset CFD simulations of wind turbine aerodynamics. Renew Energy 2012;37:285–98.
[19] Burton T, Jenkins N, Sharpe D, Bossanyi E. Wind energy handbook. 2nd ed. New York: Wiley; 2011.
[20] Habali SM, Saleh IA. Local design, testing and manufacturing of small mixed airfoil wind turbine blades of glass fiber reinforced plastics: part I: design of the blade and root. Energy Convers Manag 2000;41:249–80.
[21] Kishinami K, Taniguchi H, Suzuki J, Ibano H, Kazunou T, Turuhami M. Theoretical and experimental study on the aerodynamic characteristics of a horizontal axis wind turbine. Energy 2005;30(1112):2089–100.
[22] Imraan M, Sharma RN, Flay RG. Wind tunnel testing of a wind turbine with telescopic blades: the influence of blade extension. Energy 2013;53(0):22–32.
[23] Menter FR. Zonal two equation $k$-$\omega$ turbulence models for aerodynamic flows. In: 24th fluid dynamics conference, no. AIAA-93-2906, AIAA, Orlando, Florida, USA 1993. pp. 1–21.
[24] Menter FR. Two-equation eddy-viscosity turbulence models for engineering applications. AIAA J 1994;32:1598–605.
[25] Menter F, Esch T. Elements of industrial heat transfer predictions. In: Proceedings of COBEM 2001, invited lectures16th Brazilian congress of mechanical engineering (XVI Congresso Brasileiro de Engenharia Mecânica), vol. 20; 2001. pp. 117–27. Uberlândia, Brazil.
[26] Menter FR, Kuntz M, Langtry R. Ten years of industrial experience with the SST turbulence model. In: Turbulence, heat and mass transfer 4: proceedings of the fourth international symposium on turbulence, heat and mass transfer, turbulence heat and mass transfer series. Antalya: Begell House; 2003. pp. 625–32.
[27] Versteeg H, Malalasekera W. An introduction to computational fluid dynamics: the finite volume method. 2nd ed. Harlow: Pearson Education Limited; 2007.
[28] Weller HG, Tabor G, Jasak H, Fureby C. A tensorial approach to computational continuum mechanics using object-oriented techniques. Comput Phys 1998;12:620–31.

[29] Gebreslassie MG, Tabor GR, Belmont MR. Numerical simulation of a new type of crossflow tidal turbine using OpenFOAM Part I: calibration of energy extraction. Renew Energy 2013;50:994–1004.
[30] Jasak H, Weller H, Gosman A. High resolution NVD differencing scheme for arbitrarily unstructured meshes. Int J Numer Method Fluid 1999;31:431–49.
[31] Mohamed M. Impacts of solidity and hybrid system in small wind turbines performance. Energy 2013;57(0):495–504.
[32] Shih TH, Liou WW, Shabbir A, Yang Z, Zhu J. A new $k$-$\varepsilon$ eddy viscosity model for high Reynolds number turbulent flows. Comput Fluid 1995;24(3):227–38.